Preparation of a Promising MXene Loaded NiCo$_2$O$_4$ Complementary Nanocomposite for Supercapacitor Electrodes

Yanhua Li,[1,2] Kuo Zhang,[1,2] Dongjia Wang,[1,2] Qun Li,[1,2,*] Shuhuan Wang[1,2,#]

[1] School of Metallurgy and Energy, North China University of Science and Technology, Tangshan, Hebei, 063210, China

[2] Key Laboratory of Special Metallurgy and Material Manufacture, Tangshan, Hebei, 063210, China

[*] Corresponding author's e-mail address: liq@ncst.edu.cn

[#] Corresponding author's e-mail address: wshh88@ncst.edu.cn

Abstract: The insufficient specific capacitance of MXene limits its application in supercapacitors. To solve the problem, MXene/NiCo$_2$O$_4$ composite was designed *via* the in-situ growth of NiCo$_2$O$_4$ nanowires on MXene nanosheets. The introduction of NiCo$_2$O$_4$ nanowires composed of nanoparticles was conducive to the intercalation of MXene nanosheets and the ion permeation inside the electrode, which will enhance the electrochemical performance. As a result, the specific capacitance of the composite was greatly improved originated from reactions of M-O/M-O-OH (M = Co, Ni) and the unique hierarchical structure. The MXene/NiCo$_2$O$_4$ nanocomposite presented a higher specific capacitance of 1012 F g^{-1} at 0.5 A g^{-1} and 827.69 F g^{-1} at 1 A g^{-1} than MXene (8.7 F g^{-1} at 0.5 A g^{-1}). The specific capacitance of MXene/NiCo$_2$O$_4$ was retained as high as 84.1 % with 696 F g^{-1} at 2 A g^{-1}, which demonstrates the high rate performance. More importantly, the capacitance retention rate could be kept with 83.3 % over 1000 cycles, indicating MXene/NiCo$_2$O$_4$ has a great potential to be applied in supercapacitors. The work provides a feasible strategy for the creation and application of the high-performance composite electrode.

Keywords: nanocomposites, energy storage and conversion, supercapacitor, excellent electrochemical performance.

INTRODUCTION

SUPERCAPACITORS (SCs) are one of the most promising high-performance energy storage system devices due to high power density, fast charge and discharge rate, long cycle life, high safety and wide operating voltage range, etc,[1–3] which render them widely applicable in the storage and utilization of clean and renewable resources such as wind, hydro and solar energy.[4,5] However, the low energy density restricts their development.[6] It is well known that the rational utilization and perfect structure design of electrode material play an important role in improving the practical performance of supercapacitors.[7]

As a highly attractive electrode material for supercapacitors, MXene (Ti$_3$C$_2$) possesses the excellent metal conductivity (3300 S cm^{-1}), high mechanical strength, good hydrophilicity, layer structure and rich surface terminal groups, etc.[8–10] Since the surface of original accordion-like MXene cannot be fully utilized, its good performance will be limited. In recent years, many approaches have been explored to develop MXene nanosheets structure. Among them, LiF+HCl etchment method along with hand-shaking operation is safe, easy and frequently employed for the preparation of high-quality few layer MXene nanosheets.[11,12] However, hydrogen bonding and van der Waals forces between adjacent MXene nanosheets will lead to severe layer restacking and aggregation, and further cause the sluggish electronic kinetics.[13,14] Thus, developing a composite system with a tunable and unique structure by introducing other pseudocapacitance nanomaterials into MXene is a promising strategy to alleviate the above problem. For instance, Mathew *et al*. reported an excellent specific capacitance of 1908.5 F g^{-1} at 1 A g^{-1} based on MXene decorated by CeO$_2$, which is caused by the enlargement of MXene interlayer spacer due to the introduction of CeO$_2$.[15] Tang *et al*. also designed a supercapacitor electrode with a

high energy density of 15.71 μWh cm^{-2} based on MXene/PANI composite fiber.[16]

To our knowledge, Ni-based and Co-based metal oxides have been successfully applied in supercapacitors because of the numerous advantages including easy preparation, low cost, friendly environment and diverse morphology.[17,18] In addition, it has been found that Ni-based and Co-based metal oxides commonly exhibit high pseudo capacity during the energy storage process owing to the multivalent states of Ni and Co elements.[19–21] Particularly, $NiCo_2O_4$ manifests higher capacitance than NiO and CoO due to the existence of two groups of active centers of Co and Ni,[22] making it one of the most promising candidate materials for designing composite structures. Unfortunately, the poor conductivity and the inferior electrochemical cycle life limit its electrochemical performance.[21,23] Combining $NiCo_2O_4$ with high conductive substrate materials to construct composite electrodes with reasonable morphology and controllable composition can effectively promote the conductive capacity and maximum functional surface exposure. Meng et al.[24] prepared $NiCo_2O_4$ microspheres well-distributed on rGO nanosheets, which lead to an excellent specific capacitance of 702 F g^{-1} at 0.5 A g^{-1} and a high cycle stability. Thus it can be speculated that it is also feasible to construct MXene/$NiCo_2O_4$ composite to optimize the electrochemical performance.

In this work, the in situ-growth of NiCo-LDH nanowires on MXene nanosheets was firstly realized *via* the simple solvothermal treatment and then the MXene/$NiCo_2O_4$ composite was successfully obtained by the transformation of NiCo-LDH to $NiCo_2O_4$ under calcination. $NiCo_2O_4$ nanowires composed of numerous nanoparticles effectively expand the layer space of MXene and promote the ion diffusion between the MXene layers. Besides, MXene as the substrate can improve the electron conduction ability of the composite material. Due to the perfect synergistic effects between the components, the MXene/$NiCo_2O_4$ composite structure presents abundant active sites and efficient electrons and ion transport capacity, which can contribute to a high specific capacitance of 1012 F g^{-1} at 0.5 A g^{-1} and a good cyclic stability.

EXPERIMENTAL

Materials

Ti_3AlC_2 (*wt* % ≥ 98 %) was achieved from Laizhou Kai Kai Ceramic Materials Co., Ltd., China. Hydrochloric acid (HCl, *wt* % = 36 %), Lithium fluoride (LiF, *wt* % ≥ 99 %), Nickel nitrate hexahydrate (Ni(NO₃)₂ · 6H₂O, *wt* % ≥ 99 %), Cobalt nitrate hexahydrate (Co(NO₃)₂ · 6H₂O, *wt* % ≥ 99 %), Urea (CH₄N₂O, *wt* % ≥ 99 %), *N*-dimethylmethacrylamide (*wt* % ≥ 98 %), Potassium hydroxide (KOH, *wt* % ≥ 99.9 %) were

purchased from Shanghai Aladdin Biochemical Technology Co., Ltd., China. Acetylene black (*wt* % ≥ 99.95 %) was sourced Japan Dajin Co., Ltd., Japan. And Polyvinylidene fluoride (*wt* % ≥ 99.95 %) was gained from Acorma Co., Ltd., France. All chemicals used were of analytical grade. Deionized water was used throughout the work. The 6 M KOH electrolyte solution was obtained by dissolving 33.663 g KOH into 100 mL deionized water.

Synthesis of Few-Layer MXene Nanosheets

1 g LiF was added into 20 mL HCl (9 M) and magnetically stirred at 300 rpm for 10 min. Then 1 g Ti_3AlC_2 powder was added into the above solution and magnetically stirred at 300 rpm for 24 h at 35 °C. The gained product was cleaned with deionized water and ethanol repeatedly until pH reached neutral, and then freeze-dried to obtain few-layer MXene nanosheets.

Synthesis of MXene/NiCo-LDH, MXene/NiCo₂O₄ and MXene/Ni/Co

The synthesis procedure of the MXene/$NiCo_2O_4$ composite structure is shown in Figure 1. Firstly, 0.58 g Ni(NO₃)₂ · 6 H₂O, 1.16 g Co(NO₃)₂ · 6 H₂O and 1 g CH₄N₂O were added to the mixed solution of 20 mL deionized water and 20 mL ethanol, followed by stirring magnetically at 300 rpm for 20 min. Then 20 mg few-layer MXene was added to the above solution and stirred at 300 rpm for 10 min. The solution was transferred into a Teflon-lined stainless-steel autoclave to heat at 150 °C for 4 h. The precipitate was cleaned repeatedly with deionized water and ethanol until pH reached neutral and then freeze-dried to achieve the MXene/NiCo-LDH precursor (1-MXene/NiCo-LDH). Subsequently, to explore the effects of calcination atmosphere (air and NH₃) on the phase, morphology and electrochemical properties of the products, 1-MXene/NiCo-LDH precursor was calcined in a tubular furnace at 400 °C
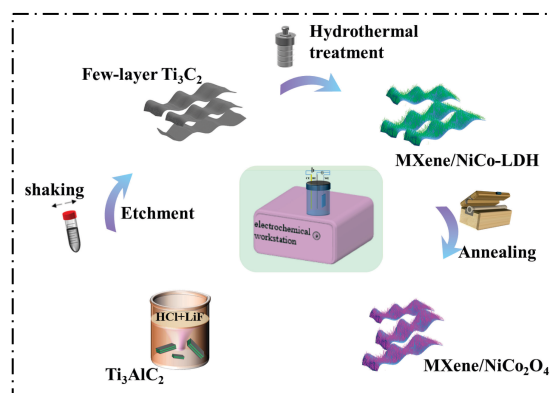

Figure 1. The synthesis procedure of the MXene/$NiCo_2O_4$ composite structure.

for 2 h in air and NH₃ atmosphere to obtain the MXene/NiCo₂O₄ and MXene/Ni/Co composite structure, respectively. For comparison, 2-MXene/NiCo-LDH precursor was also prepared by adjusting the addition amount of MXene to 40 mg.

Preparation Process of the Modified Electrode

The glassy carbon (GC) electrode with a diameter of 3 mm was firstly polished with 0.3 and 0.05 μm alumina slurry sequentially and then washed ultrasonically in water and ethanol for a few minutes, respectively. Then the cleaned GC electrode was dried in nitrogen steam for next modification. Active material, PVDF and acetylene black with the mass ratio of 8 : 1 : 1 were dispersed in DMF by strong sonication to from a stable suspension. The concentration of active material in the suspension was 3 mg mL⁻¹. Then, 3 μL of the suspension was spread evenly on the surface of GC electrode, followed by natural air drying. The mass of active material on the GC electrode is about 0.009 mg.

Material Characterization

X-ray diffractometer (XRD, Smartlab, Rigaku, Japan) was applied to test the phase composition with Cu target with scan rate of 10° min⁻¹ ($\lambda_{CuK\alpha}$ = 0.15418 nm). The microstructure and crystal structure of the samples were observed by scanning electron microscopy (FE-SEM, Quanta 650 FEG, FEI, USA) and high-resolution transmission electron microscopy (HRTEM, JEM-2100Plus, JEOL, Japan, 200 kV). The element distribution of the samples was characterized by energy dispersive spectrometer (EDS). X-ray photoelectron spectrometer (XPS, 3K-Alpha, Thermo Scientific, Al Kalpha) was used to detect chemical states on the surface of the samples. The specific surface area and pore size distribution were characterized by nitrogen absorption and desorption experiments (ASAP 2460, USA) at 77 K. The specific surface area was calculated by Bruner-Emmett-Teller (BET) model. The pore size distribution was obtained by Barret-Joyner-Halenda (BJH) method.

Electrochemical Characterization

The electrochemical performance of the samples was tested by an electrochemical workstation (Chenhua, CHI760E). And the electrochemical characterizations in the work were performed at the room temperature. The platinum electrode was applied as the counter electrode, and the Hg/HgO electrode was utilized as the reference electrode with 6 M KOH as the electrolyte. The potential with respect to the standard hydrogen electrode (SHE) of the Hg/HgO electrode in 6 M KOH electrolyte is approximately +0.098 V. The cyclic voltammetry curves (CV, –0.2–0.45 V) at different scan rates, galvanostatic charge-

discharge curves (GCD, –0.2–0.45 V) at different specific currents and the electrochemical impedance spectroscopy curves (EIS, ±5 mV, 100 KHz–0.01 Hz) were recorded by a three-electrode system. The specific capacitance of the active material was calculated by Eq. (1).[25]

$$C_s = \frac{I \cdot \Delta t}{m \cdot \Delta U} \qquad (1)$$

Where C_s (F g⁻¹), I (A), Δt (s), m (g) and ΔU (V) represent the specific capacitance, discharge current, discharge time, mass of the active material loaded on the working electrode and the working voltage window.

RESULTS AND DISCUSSION

Structural and Morphological Characterization

In Figure 2a, the XRD of MXene exhibits an obvious diffraction peak representing the (002) plane located at 2ϑ = 6.92° and other small peaks located at 2ϑ = 14.15, 20.96, 28.47, 35.70 and 60.72, corresponding to the (004), (006), (008), (0010) and (110) plane of MXene, respectively, illustrating the high purity of the prepared MXene, which is consistent with the previous work.[26,27] As for the MXene/NiCo-LDH precursor, all characteristic peaks of the MXene/NiCo-LDH precursor correspond to Co(CO₃)₀.₅(OH)₀.₁₁H₂O (JCPDS-48-0083) except for the characteristic peak of (002) plane of MXene. The partial substitution of Co by Ni will not change the crystal structure.[28] It is worth noting that the characteristic peaks of (002) plane of MXene/NiCo-LDH precursors significantly shift to lower angles than pure MXene, which proves the expansion of MXene layer space after the growth of NiCo-LDH.[29] The intercalation of NiCo-LDH into MXene is beneficial to promote the ion transport.

Figure 2b indicates 1-MXene/NiCo-LDH successfully transforms to MXene/NiCo₂O₄ and MXene/Ni/Co via the calcination in air atmosphere and NH₃ atmosphere, respectively. It may because that Ni and Co present low valence states under the reduction effects of NH₃. In addition, the (002) plane of MXene can not be found after calcination, which may be caused by the blocking effect of NiCo₂O₄ with higher peak intensity.[30] And there is a weak peak after calcination in air located at 2ϑ = 25° corresponding to TiO₂ (1-562-TiO₂), indicating the slight oxidation phenomenon of MXene.

The full-range spectra (Figure 2c) of MXene/NiCo₂O₄ manifests the existence of C 1s, Ti 2p, O 1s, Co 2p and Ni 2p. In high-resolution Ti 2p spectra (Figure 3d), the peaks at 457.65 eV (462.6 eV) and 458.85 eV (464.55 eV) can be indexed to C-Ti and TiO₂, respectively, which indicates Ti₃C₂ is partially oxidized to TiO₂.[31] In Figure 2e, the Ni 2p spectra displays the Ni 2p₁/₂, Ni 2p₃/₂ and two satellite peaks.
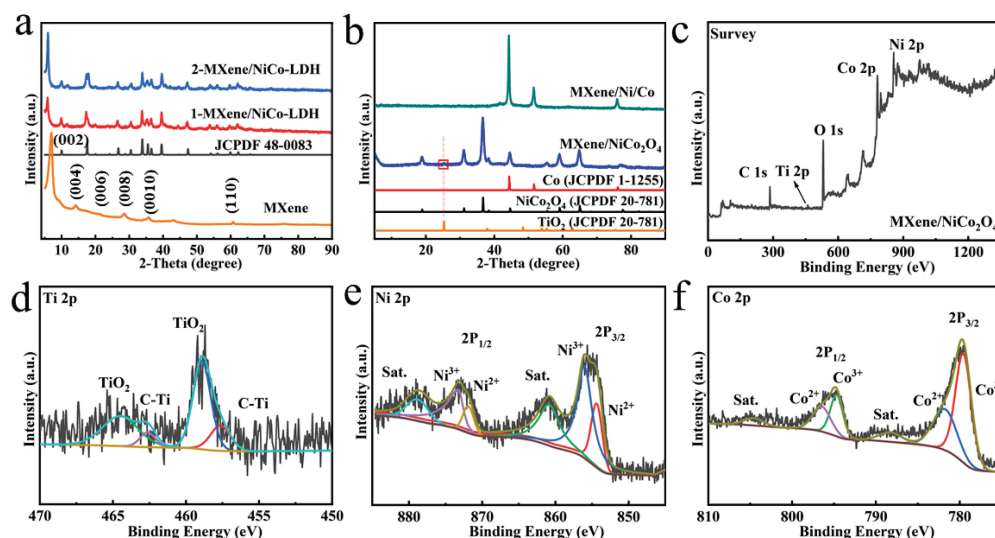
Figure 2. a,b) XRD patterns of as-prepared samples, c–f) Full-range spectra, the high-resolution Ti 2p spectra, the high-resolution Ni 2p spectra and the high-resolution Co 2p spectra of MXene/NiCo₂O₄.

The peaks fitting at 873.50 eV (856.10 eV) and 872.05 eV (854.45 eV) correspond well to the Ni^{3+} and Ni^{2+}, respectively.[32] Similarly, the Co 2p spectra demonstrates the peaks at 779.65 eV (794.75 eV) and 781.95 eV (796.50 eV) can be attributed to Co^{3+} and Co^{2+}, respectively (Figure 2f).[32] The multivalent states of Ni and Co are beneficial to abundant pseudocapacitive reactions.

The morphology and structure of MXene/NiCo-LDH was further optimized. Figure 3a–c show the SEM images of MXene, 2-MXene/NiCo-LDH and 1-MXene/NiCo-LDH, respectively. Figure 3a demonstrates the successful preparation of few-layer MXene nanosheets. From Figures 3b and 3c, it can be clearly observed that MXene nanosheets are covered by interlacing nanowires, indicating NiCo-LDH nanowires in-situ grow on the surface of MXene for 2-MXene/NiCo-LDH and 1-MXene/NiCo-LDH, which will expand the interlayer space of MXene and promote the ion transport. By comparison, a small amount of NiCo-LDH nanowires load on the surface of MXene (Figure 3b) for 2-MXene/NiCo-LDH. While sufficient NiCo-LDH nanowires uniformly distribute on MXene surface for 1-MXene/NiCo-LDH (Figure 3c), which are more

conducive to provide large specific surface area and abundant active sites for improving electrochemical performance. Thus, 1-MXene/NiCo-LDH is selected and used for further study.

The microstructure and morphology of MXene/NiCo₂O₄ was characterized in Figure 4a–e. From the SEM image in Figure 4a, it can be seen that the structure of MXene/NiCo₂O₄ is maintained well after the calcination in air. Figure 4b further confirms the growth of NiCo₂O₄ nanowires on MXene nanosheets. Figure 4c indicates that NiCo₂O₄ nanowires are composed of a large number of nanoparticles with a diameter of about 15 nm, which is caused by the grain size shrink of the nanoparticles comprising the NiCo-LDH nanowires due to the release of CO_2 and H_2O during the heat treatment process.[28] The structure will lead to many pores existing among the nanoparticles, which will provide an effective ion transport pathway to facilitate the penetration and diffusion of electrolyte ion within the composite electrode. In Figure 4d, the space between the defined lattice fringe is measured to be 0.27 nm, corresponding to the (311) crystal plane of NiCo₂O₄. The SAED pattern with different sizes in
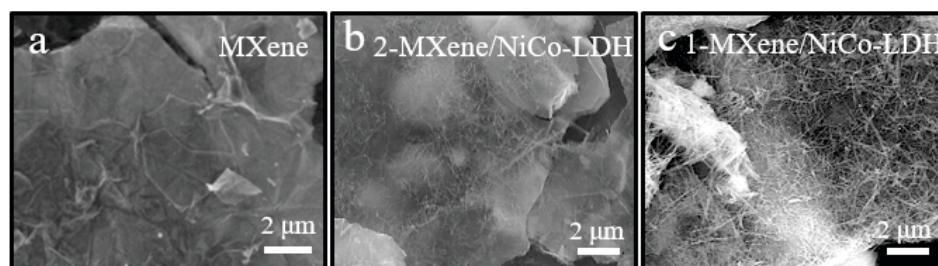

Figure 3. a–c) SEM images of MXene, 2-MXene/NiCo-LDH and 1-MXene/NiCo-LDH.

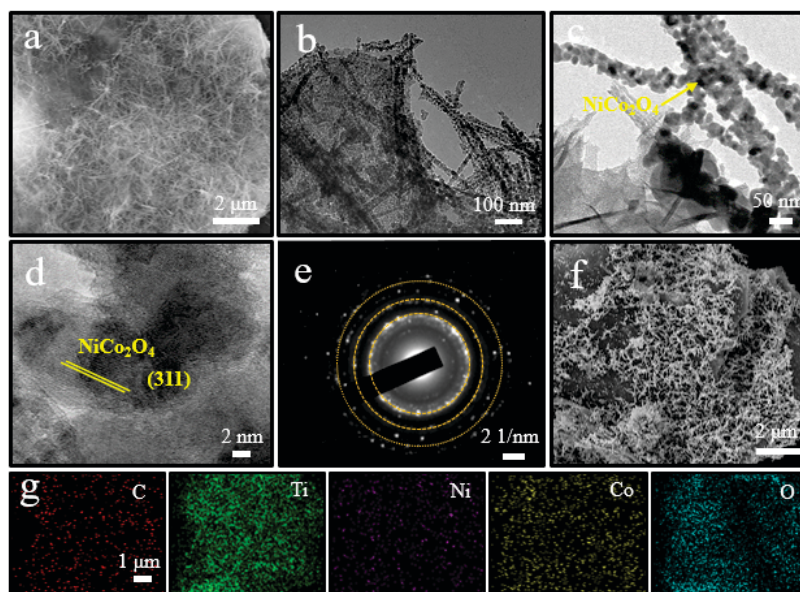**Figure 4.** a) SEM image, b-d) TEM images,e) SAED pattern of MXene/NiCo$_2$O$_4$, (f) SEM image of MXene/Ni/Co, g) Elemental map of MXene/NiCo$_2$O$_4$.
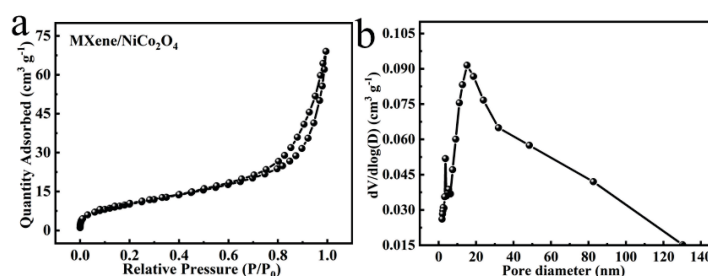

Figure 5. a) N$_2$ physical adsorption/desorption isotherm and b) pore size distribution of MXene/NiCo$_2$O$_4$.

Figure 4e show the polycrystalline characteristics of MXene/NiCo$_2$O$_4$.[29] Figure 4f exhibits the morphology of MXene/Ni/Co. Compared with MXene/NiCo$_2$O$_4$, the Ni/Co nanowires on MXene become distinctly curly after NH$_3$ treatment and can not maintain the inherent morphology of NiCo-LDH nanowires, indicating the efficient electron transport path will be destructed, which go against the pseudocapacitance reactions and the energy storage. Thus, the MXene/NiCo$_2$O$_4$ structure is more potential for supercapacitor than MXene/Ni/Co. The element map of MXene/NiCo$_2$O$_4$ (Figure 4g) shows the homogeneous distribution of C, Ti, Ni, Co and O elements, further revealing the successful synthesis of MXene/NiCo$_2$O$_4$.

The N$_2$ adsorption-desorption isotherm and pore size distribution of MXene/NiCo$_2$O$_4$ are displayed in Figure 5a,b, respectively. MXene/NiCo$_2$O$_4$ possesses a high active surface area of 36.3 m^2 g^{-1}. Based on the International Union of Pure and Applied Chemistry (IUPAC), Figure 5a displays a type-IV isotherm with a hysteresis loop located
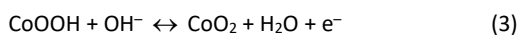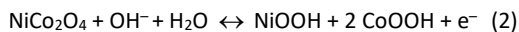
at the range of 0.8–1.0, which confirms the presence of mesoporous. Besides, Figure 5b further indicates the massive pores exist in the composite, which can effectively accelerate the ion diffusion for further improving electrochemical performance.

Electrochemical Performances of as-Prepared Samples

The electrochemical performance of MXene, 1-MXene/NiCo-LDH and 2-MXene/NiCo-LDH is compared shown in Figure 6a. The larger closed pattern area represents higher specific capacitance. It can be seen that the specific capacitance of 1-MXene/NiCo-LDH is significantly higher than that of 2-MXene/NiCo-LDH, which can be attributed to more redox reactions caused by the sufficient NiCo-LDH nanowires.

In Figure 6b, MXene/NiCo$_2$O$_4$ shows highest specific capacitance than 1-MXene/NiCo-LDH and MXene. Besides, the CV curve of MXene/NiCo$_2$O$_4$ displays a pair of redox

peaks originated from faradaic reactions of Co^{3+}/Co^{4+} and Ni^{2+}/Ni^{3+}.[33] This is because that the redox potential of Co^{3+}/Co^{4+} and Ni^{2+}/Ni^{3+} transitions are so close, so there is only one pair of redox peaks can be visible.[33] The reaction processes are described as chemical reaction [Eq. (2) and Eq. (3)].

$$NiCo_2O_4 + OH^- + H_2O \leftrightarrow NiOOH + 2\ CoOOH + e^- \quad (2)$$

$$CoOOH + OH^- \leftrightarrow CoO_2 + H_2O + e^- \quad (3)$$

In Figure 6c, MXene/NiCo₂O₄ signifies highest discharge time compared with 1-MXene/NiCo-LDH and MXene. The charge and discharge platform expressed by the GCD curve of MXene/NiCo₂O₄ correspond to the redox peaks of the CV curve. The raised specific capacitance of MXene/NiCo₂O₄ can be ascribed to the existence of numerous pores and abundant active sites, facilitating the adsorption and transport of electrolyte ions. Besides, the occurrence of numerous redox reactions originated from Ni and Co ions during charge and discharge also result in higher energy storage. The specific capacitance of MXene/NiCo₂O₄ is calculated to be 1012 F g⁻¹ at the specific current of 0.5 A g⁻¹.

As for MXene/NiCo₂O₄, the CV curves display the almost similar shape and increased closed pattern area with the increase of scan rates, which clarifies the fast charge and discharge behavior[34] and reversible charge/discharge capability (Figure 6d). The oxidation peak and reduction peak of CV curves shift positively and negatively, respectively, owing to the increased ion diffusion resistance at high scan rates.[35] Figure 6e indicates the GCD curves at different specific currents show approximate triangles and symmetrical shapes, which confirms the good reversibility,[36] consistent with outcome of CV tests. And the voltage drop in all GCD curves can be neglected, which indicate the good ionic and electronic conductivity.[36]

The Nyquist plots of MXene/NiCo₂O₄ and 1-MXene/NiCo-LDH are shown in Figure 6f. Compared with 1-MXene/NiCo-LDH, the intercept of the Nyquist plot of MXene/NiCo₂O₄ with the real axis in the high frequency region is lower, indicating its lower equivalent series resistance.[37] In addition, higher slope of MXene/NiCo₂O₄ in the low frequency region represents lower ion transport resistance and the large pseudocapacitive behavior.[38] Based on Figure 6e, the specific capacitances at different specific currents are calculated and displayed in Figure 6g. The specific capacitances of MXene/NiCo₂O₄ at 1 A g⁻¹ and 2 A g⁻¹ is 827.69 F g⁻¹ and 696 F g⁻¹, respectively. The specific capacitance retention can be maintained as 84.1 % at 2 A g⁻¹, which proves the good rate performance. Cyclic stability is a key parameter to measure the practicality of the electrode materials. The cyclic stability of MXene/NiCo₂O₄ is shown in Figure 6h. The specific capacitance retention of
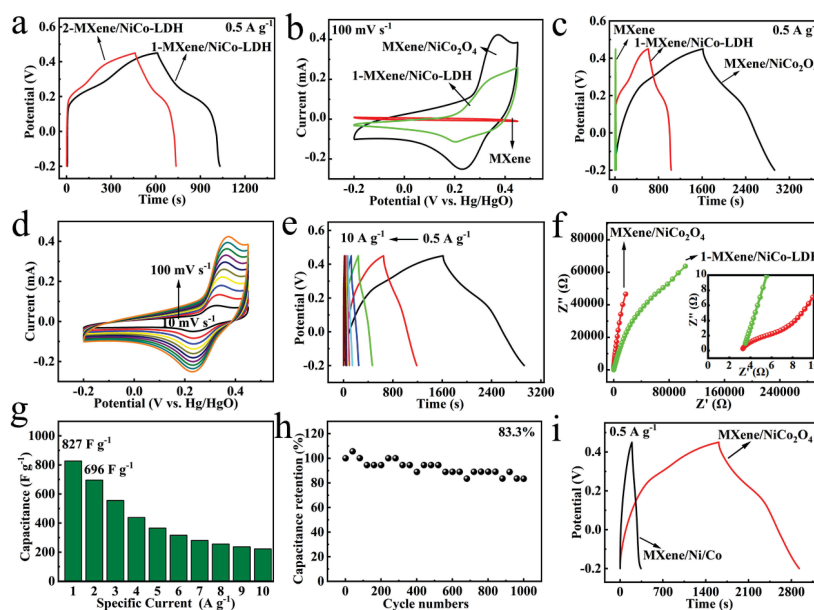

Figure 6. a) GCD curves of 1-MXene/NiCo-LDH and 2-MXene/NiCo-LDH at 0.5 A g⁻¹, b,c) CV curves at 100 mV s⁻¹ and GCD curves at 0.5 A g⁻¹ of MXene, 1-MXene/NiCo-LDH and MXene/NiCo₂O₄, d,e) CV curves and GCD curves of MXene/NiCo₂O₄ at different scan rates and different specific currents, f) Nyquist plots of MXene/NiCo₂O₄ and 1-MXene/NiCo-LDH, g,h) Specific capacitances at different specific currents and Cyclic stability for 1000 cycles of MXene/NiCo₂O₄, i) GCD curves of MXene/NiCo₂O₄ and MXene/Ni/Co at 0.5 A g⁻¹.
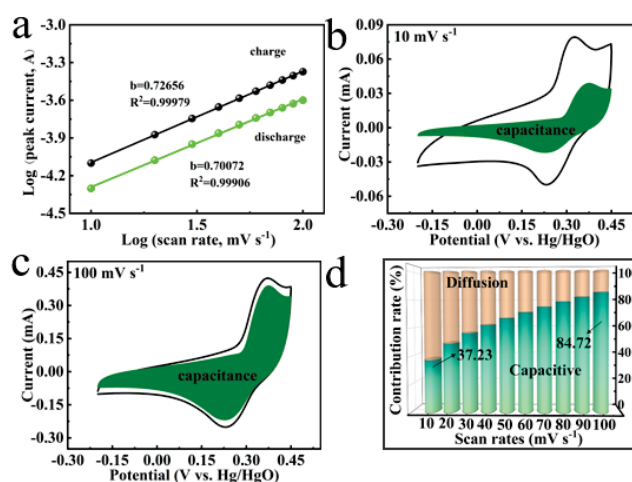
Figure 7. a) The relationship between peak currents and scan rates, b,c) contribution rates of surface capacitive process at 10 mV s⁻¹ and 100 mV s⁻¹, d) contribution rates of surface capacitive process at different scan rates of MXene/NiCo₂O₄.

MXene/NiCo₂O₄ can be retained to 83.3 % after 1000 cycles. And the specific capacitance increases slightly in the first 50 cycles, caused by the electrode activation and the gradual penetration of the electrolyte into the active material.[39]

The electrochemical performance of MXene/NiCo₂O₄ and MXene/Ni/Co are compared in Figure 6i. The specific capacitance of MXene/Ni/Co is lower than that of MXene/NiCo₂O₄ due to the destruction of nanowire structures and the transport path of electrons and ions.

According to Dunn's method,[40] the electrochemical reaction kinetics and energy storage mechanism of the composite electrode can be further explored based on the relationship between the peak current (I, A) and the scan rate (v, mV s⁻¹) in the CV curves described by [Eq. (4)][41,42]:

$$I = I_{capacitive} + I_{diffusion} = ay^b \qquad (4)$$

where a is a constant, b is a variable parameter. "$b = 0.5$" represents the diffusion-controlled process indicating a battery-type material, and "$b = 1$" represents the surface capacitance process. Based on the functional relationship between logarithm peak current ($\log(I)$) and logarithm scan rate ($\log(v)$) in Figure 7a, the b value of MXene/NiCo₂O₄ is calculated to be 0.73 in the charge process and 0.70 in the discharge process, indicating that the energy storage is determined by both diffusion-controlled process and surface capacitance process. What's more, the quantitative contributions of surface capacitive process ($k_1 v$) and diffusion-controlled process ($k_2 v^{1/2}$) at different scan rates are analyzed based on [Eq. (5)][41,42] by plotting $v^{1/2}$ versus $I / v^{1/2}$.

$$I = k_1 v + k_2 v^{1/2} \qquad (5)$$

where k_1 and k_2 represent the slope and intercept of the plot of $I / v^{1/2}$ versus $v^{1/2}$, respectively. Figure 7b–c show the contribution rate of surface capacitance process at 10 mV s⁻¹ and 100 mV s⁻¹ is 37.23 % and 84.72 %, respectively. It can be observed that the contribution rate of surface capacitance presents a rising trend with the

Table 1. Electrochemical performances of Ni-based, Co-based and Ti₃C₂-based composite materials for supercapacitor application in a three-electrode system.

Electrode material	Electrolyte	Potential (V)	Capacitance	Rate capability	Cyclic stability	Ref
Ti₃C₂Tₓ/NiCo-LDH	1 M KOH	0–0.6	136.9 F cm⁻² at 0.5 mA cm⁻²	–	74.2 % (7000)	[43]
MXene/Ni(OH)₂/NF	1 M KOH	0–0.7	0.223 mAh cm⁻² at 1 mA cm⁻²	71 % (5 mA cm⁻²)	83.62 % (5000)	[44]
CoO/NiCo-LDH	3 M KOH	0–0.6	440.19 C g⁻¹ at 0.28 A g⁻¹	–	88.76 % (5000)	[45]
Mo₁.₅NiCo-LDH@Co-N/C@MX/CF	2 M KOH	0–0.5	4.55 mF cm⁻² at 3.86 mA cm⁻²	–	83.5 % (5000)	[46]
P-Ti₃C₂@NiCo₂S₄	3 M KOH	−1–0.4	973 F g⁻¹ at 1 A g⁻¹	–	67.57 % (4000)	[47]
NiCo₂O₄/Ti₃C₂	6 M KOH	−0.2–0.45	1012 F g⁻¹ at 0.5 A g⁻¹ 827.69 F g⁻¹ at 1 A g⁻¹	84.1 % (2 A g⁻¹)	83.3 % (1000)	This work

increase of scan rates (Figure 7d), which can be ascribed to the diffusion delay of electrolyte ions to the inner electrode at high scan rates.[7]

Based on the above results, the preferable electrochemical performance of MXene/NiCo₂O₄ can be explained as follows. The highly conductive MXene substrate promotes the uniform distribution of NiCo₂O₄ and improves its conductive capacity. And the introduction of NiCo₂O₄ nanowires significantly enhances the specific capacitance of the composite. In view of the complementary and synergistic effects between NiCo₂O₄ and MXene, the ultimate MXene/NiCo₂O₄ electrode exhibits an excellent electrochemical performance, which is compared to the previous Ni-based, Co-based and Ti₃C₂-based composite materials, as shown in Table 1.[43–47] The achievements related to specific capacitance, rate capability and cyclic stability in our work manifest a high level.

CONCLUSION

In summary, MXene/NiCo₂O₄ was constructed by the simple hydrothermal treatment for the load of the NiCo-LDH precursor on MXene and the subsequent calcination in air for the transformation from NiCo-LDH to NiCo₂O₄. Multiple techniques including XRD, SEM, TEM and BET characterizations were applied to explore the obtained MXene/NiCo₂O₄ composite. NiCo₂O₄ is characterized as nanowires structure with a diameter of about 15 nm and is assembled from a large number of nanoparticles. MXene nanosheets act as a conductive substrate can facilitate the conductivity and the uniform distribution of NiCo₂O₄ nanowires. Besides, the introduction of NiCo₂O₄ nanowires composed of nanoparticles will provide massive pores and abundant specific surface area for MXene/NiCo₂O₄, which will promote the transport of electrolyte ions and the faradaic reactions of Ni and Co ions. Based on this, MXene/NiCo₂O₄ is employed as electrode materials to evaluate the electrochemical performance. As a result, MXene/NiCo₂O₄ exhibits obviously better electrochemical performance than MXene. The gained MXene/NiCo₂O₄ composite material demonstrates a high specific capacitance of 1012 F g^{-1} at 0.5 A g^{-1} and 827.69 F g^{-1} at 1 A g^{-1}, and a good rate performance. In addition, the composite shows a satisfactory durability with a specific capacitance retention of 83.3 % over 1000 cycles at a specific current of 15 A g^{-1}. The work verifies that the novel MXene/NiCo₂O₄ composite will be a potential candidate for the development of energy storage devices.

REFERENCES

[1] Y. X. Wang, T. Xu, K. Liu, M. Zhang, X. M. Cai, C. L. Si, *Aggregate* **2024**, *5*, e428.
https://doi.org/10.1002/agt2.428

[2] W. Raza, F. Ali, N. Raza, Y. W. Luo, K. H. Kim, J. H. Yang, S. Kumar, A. Mehmood, E. E. Kwon, *Nano Energy* **2018**, *52*, 441–473.
https://doi.org/10.1016/j.nanoen.2018.08.013

[3] S. S. Shah, M. A. Aziz, M. M. Al, A. Z. Khan, Z. H. Yamani, *J. Power Sources* **2024**, *602*, 234334.
https://doi.org/10.1016/j.jpowsour.2024.234334

[4] R. Manzar, M. Saeed, U. Shahzad, J. Y. Al-Humaidi, S. U. Rehman, R. H. Althomali, M. M. Rahman, *Prog. Mater. Sci.* **2024**, *144*, 101286.
https://doi.org/10.1016/j.pmatsci.2024.101286

[5] J. Ran, Y. F. Liu, H. X. Feng, H. X. Shi, Q. Ma, *Ind. Eng. Chem.* **2024**, *137*, 106–121.
https://doi.org/10.1016/j.jiec.2024.03.043

[6] V. Molahalli, K. Chaithrashree, M. K. Singh, M. Agrawal, S. G. Krishnan, G. Hegde, *J. Energy Storage* **2023**, *70*, 108062.
https://doi.org/10.1016/j.est.2023.108062

[7] M. Hussain, B. M. Alotaibi, A. W. Alrowaily, H. A. Alyousef, M. F. Alotiby, M. Abdullah, A. G. Al-Sehemi, A. M. A. Henaish, Z. Ahmad, S. Aman, *J. Phys. Chem. Solids* **2024**, *188*, 111919.
https://doi.org/10.1016/j.jpcs.2024.111919

[8] W. Fan, Q. Wang, K. Rong, Y. Shi, W. Peng, H. D. Li, Z. H. Guo, B. B. Xu, H. Hou, H. Algadi, S. Ge, *Nanomicro Lett.* **2024**, *16*, 36.
https://doi.org/10.1007/s40820-023-01226-y

[9] Y. Wang, Y. Yuan, H. Geng, W. Yang, X. Chen, *Adv. Funct. Mater.* **2024**, 2400887.
https://doi.org/10.1002/adfm.202400887

[10] M. N. Mustafa, M. A. A. M. Abdah, N. M. Saidi, W. P. Wong, Y. S. Tan, A. Numan, Y. Sulaiman, R. Walvekar, F. N. M. Azlan, M. Khalid, *J. Power Sources* **2024**, *595*, 234079.
https://doi.org/10.1016/j.jpowsour.2024.234079

[11] T. Zhang, L. Pan, H. Tang, F. Du, Y. Guo, T. Qiu, J. Yang, *J. Alloys Compd.* **2017**, *695*, 818–826.
https://doi.org/10.1016/j.jallcom.2016.10.127

[12] M. Alhabeb, K. Maleski, B. Anasori, P. Lelyukh, L. Clark, S. Sin, Y. Gogotsi, *Chem. Mater.* **2017**, *29*, 7633–7644.
https://doi.org/10.1021/acs.chemmater.7b02847

[13] M. Rostami, P. Rezvaninia, A. Amiri, G. M. Ziarani, M. R. Ganjali, A. Badiei, *Results Eng.* **2024**, *22*, 102227. https://doi.org/10.1016/j.rineng.2024.102227

[14] M. Shariq, S. Marimuthu, A. R. Dixit, S. Chattopadhyaya, S. Pandiaraj, M. Muthuramamoorthy, A. N. Alodhyab, M. K. Nazeeruddin, A. N. Grace, *Chem. Eng. J.* **2024**, *484*, 149502. https://doi.org/10.1016/j.cej.2024.149502

[15] S. Mathew, S. D. KR, *Colloids Surf., A* **2024**, *684*, 133170. https://doi.org/10.1016/j.colsurfa.2024.133170

[16] J. H. Tang, X. H. Zheng, B. B. Ding,L. H. Zou, P. Wang, C. L. Li, X. H. Hong, Z. Q. Wang, *Mater. Lett.* **2024**, *355*, 135494. https://doi.org/10.1016/j.matlet.2023.135494

[17] R. A. Senthil, A. Min, J. Theerthagiri, G. A. Kim, H. C. Choi, M. Y. Choi, *J. Energy Storage*, **2023**, *72*, 108305. https://doi.org/10.1016/j.est.2023.108305

[18] Q. Abbas, H. Khurshid, R. Yoosuf, J. Lawrence, B. A. Issa, M. A. Abdelkareem, A. G. Olabi, *SCI.* Rep. **2023**, *13*, 15654. https://doi.org/10.1038/s41598-023-42647-4

[19] Y. F. Lin, S. Zhang, L. X. Guan, J. H. Tao, *J. Mater. Sci.* **2021**, *56*, 1897–1918. https://doi.org/10.1007/s10853-020-05408-6

[20] J. F. Pan, C. H. Li, Y. T. Peng, L. L. Wang, B. T. Li, G. X. Zheng, M. X. Song, *Int. J. Electrochem. Sci.* **2023**, *18*, 100233. https://doi.org/10.1016/j.ijoes.2023.100233

[21] X. Wei, X. R. Zhou, L. L. Li, W. Z. Feng, H. Y. Wu, *Appl. Surf. Sci.* **2023**, *613*, 155959. https://doi.org/10.1016/j.apsusc.2022.155959

[22] W. Cao, W. J. Zhao, C. H. Xiong, Q. Long, N. Chen, G. P. Du. *J. Energy Storage* **2023**, *64*, 107213. https://doi.org/10.1016/j.est.2023.107213

[23] T. T. Jiang, X. L. Wang, H. Zhou, R. Nasser, D. H. Wu, J. M. Song, *J. Energy Storage* **2023**, *72*, 108184. https://doi.org/10.1016/j.est.2023.108184

[24] F. B. Meng, L. C. Zhao, Y. J. Zhang, J. Zhai, Y. J. Li, W. Zhang, *Ceram. Int.* **2019**, *45*, 23701–23706. https://doi.org/10.1016/j.ceramint.2019.08.085

[25] P. Salarizadeh, M. B. Askari, M. Seifi, S. M. Rozati, S. S. Eisazadeh, *Mater. Sci. Semicond. Process.* **2020**, *114*, 105078. https://doi.org/10.1016/j.mssp.2020.105078

[26] Y. D. Wei, M. M. Zheng, W. L. Luo, B. Dai, J. J. Ren, M. L. Ma, T. X. Li, Y. Ma, *J. Energy Storage* **2022**, *45*, 103715. https://doi.org/10.1016/j.est.2021.103715

[27] W. Li, Z. Y. Xu, Y. Yan, Q. F. Gao, Y. Y. Song, J. Wang, M. B. Zhang, J. M. Xue, S. Z. Xu, Y. Ding, X. L. Chen, X. Y. Li, L. P. Zhang, Q. Huang, W. Z. Liu, X. D. Zhang, Y. Zhao, G. F. Hou, *small* **2024**, 2406397. https://doi.org/10.1002/smll.202406397

[28] L. N. Sha, K. Ye, G. Wang, J. Q. Shao, K. Zhu, K. Cheng, J. Yan, G. L. Wang, D. X. Cao, *J. Power Sources* **2019**, *412*, 265–271. https://doi.org/10.1016/j.jpowsour.2018.11.059

[29] Y. H. Li, S. H. Wang, G. L. Ni, Q. Li, *Molecules* **2022**, *27*, 6452. https://doi.org/10.3390/molecules27196452

[30] X. M. Li, Z. L. Zhang, Q. K. Xiang, R. R. Chen, D. Wu, G. Y. Li, L. J. Wang, *RSC Adv.* **2021**, *11*, 12392–12397. https://doi.org/10.1039/d1ra01368h

[31] C. Zhao, X. J. Zeng, R. H. Yu, Synth. Met. **2023**, *297*, 117402. https://doi.org/10.1016/j.synthmet.2023.117402

[32] T. T. Yu, S. B. Li, L. Zhang, F. B. Li, H. Pan, D. Q. Zhang, *J. Energy Storage* **2024**, *87*, 111427. https://doi.org/10.1016/j.est.2024.111427

[33] S. P. Ghaemi, S. M. Masoudpanah, S. Alamolhoda, *J. Energy Storage* **2023**, *67*, 107635. https://doi.org/10.1016/j.est.2023.107635

[34] M. A. Yewale, R. A. Kadam, N. K. Kaushik, J. R. Koduru, N. B. Velhal, U. T. Nakate, A. A. Jadhavar, N. D. Sali, D. K. Shin, *Mater. Sci. Eng. B* **2023**, *287*, 116072. https://doi.org/10.1016/j.mseb.2022.116072

[35] P. Sivakumar, C. J. Raj, H. Jung, H. S. Park, *J. Energy Storage* **2023**, *69*, 107946. https://doi.org/10.1016/j.est.2023.107946

[36] B. L. Shen, X. L. Liao, X. F. Zhang, H. T. Ren, J. H. Lin, C. W. Lou, T. T. Li, *Appl. Surf. Sci.* **2023**, *609*, 155189. https://doi.org/10.1016/j.apsusc.2022.155189

[37] H. Chen, L. F. Hu, M. Chen, Y. Yan, L. M. Wu, *Adv. Funct. Mater.* **2014**, *24*, 934–942. https://doi.org/10.1002/adfm.201301747

[38] S. Yadav, A. S. Ghrera, A. Devi, A. Rana, *Electrochim. Acta* **2023**, *437*, 141526. https://doi.org/10.1016/j.electacta.2022.141526

[39] R. Q. Liu, S. S. Xu, X. X. Shao, Y. Wen, X. R. Shi, L. P. Huang, M. Hong, J. Hu, Z. Yang, *ACS Appl. Mater. Interfaces* **2021**, *13*, 47717–47727. https://doi.org/10.1021/acsami.1c15824

[40] W. Lu, J. L. Shen, P. Zhang, Y. J. Zhong, Y. Hu, X. W. D. Lou, *Angew. Chem.* **2019**, *131*, 15587–15593. https://doi.org/10.1002/anie.201907516

[41] P. F. Huang, H. j. Ying, S. L. Zhang, Z. Zhang, W. Q. Han, *Chem. Eng. J.* **2022**, *429*, 132396. https://doi.org/10.1016/j.cej.2021.132396

[42] M. Cai, X. C. Wei, H. F. Huang, F. L. Yuan, C. Li, S. K. Xu, X. Q. Liang, W. Z. Zhou, J. Guo, *Chem. Eng. J.* **2023**, *458*, 141338. https://doi.org/10.1016/j.cej.2023.141338

[43] M. Y. Jung, C.Y. Lee, J. Park, J. W. Son, Y. J. Yun, Y. Jun, *Chem. Eng. J.* **2024**, *490*, 151556. https://doi.org/10.1016/j.cej.2024.151556

[44] X. Y. Liu, Q. Q. Fu, Z. C. Li, H. Wang, J. W. Ren, *Diamond Relat. Mater.* **2023**, *140*, 110474. https://doi.org/10.1016/j.diamond.2023.110474

[45] Z. C. Jiao, Y. Q. Chen, M. Du, M. Demir, F. X. Yan, W. M. Xia, Y. Zhang, C. Wang, M. M. Gu, X. X. Zhang, J. T. Zou, *J. Colloid Interface Sci.* **2023**, *633*, 723–736. https://doi.org/10.1016/j.jcis.2022.11.131

[46] D. D. Khumujam, T. Kshetri, T. I. Singh, N. H. Kim, J. H. Lee, *Adv. Funct. Mater.* **2023**, *33*, 2302388. https://doi.org/10.1002/adfm.202302388

[47] W. L. Wu, C. H. Zhao, J. F. Zhu, D. J. Niu, D. Wei, C. W. Wang, F. Wang, L. Wang, *Ceram. Int.* **2020**, *46*, 12200–12208. https://doi.org/10.1016/j.ceramint.2020.01.267